

## Shear wave anisotropy beneath the Taiwan orogen

Ruey-Juin Rau<sup>a,\*</sup>, Wen-Tzong Liang<sup>b</sup>, Honn Kao<sup>b</sup>, Bor-Shouh Huang<sup>b</sup>

<sup>a</sup> *Satellite Geoinformatics Research Center, National Cheng Kung University, Tainan, Taiwan*

<sup>b</sup> *Institute of Earth Sciences, Academia Sinica, Taipei, Taiwan*

Received 10 October 1999; received in revised form 14 February 2000; accepted 14 February 2000

### Abstract

Shear wave splitting in regional and teleseismic shear waves (ScS and S) has been analyzed for fast polarization directions and delay times at 33 short-period and 17 broad-band permanent and temporary seismic stations in the Taiwan region. The orientations of anisotropy for the Taiwan stations are generally parallel to the strike of the mountain belt, with a clockwise rotation following the trend of regional geologic fabric in north Taiwan. The delay times, on the other hand, vary greatly from 0.5 to 2.1 s; the largest values are from the southwestern Taiwan foothills, and an abrupt change in delay times is found in south Taiwan. The main source of shear wave splitting in Taiwan is compatible with an anisotropic region between 25 and 230 km depths. The observed splitting parameters are consistent with upper mantle anisotropy resulting from the collisional tectonics that built the Taiwan orogen. © 2000 Published by Elsevier Science B.V. All rights reserved.

*Keywords:* S-waves; wave splitting; Taiwan; lithosphere; plate collision; subduction

### 1. Introduction

Taiwan is a unique product of oblique convergence between the northeast-trending Chinese continental margin of the Eurasian plate and the north-trending Luzon arc of the Philippine Sea plate (Fig. 1; [1]). Across Taiwan, the relative plate motion between the Eurasian plate and the Philippine Sea plate is directed N54°W at an estimated rate of 8.2 cm/yr [2]. Based on seismicity, bathymetric, topographic and structural patterns, the tectonic processes in Taiwan are characterized by an active collision orogen intervening between

two subduction systems, the Ryukyu arc and the Luzon arc to the northeast and south, respectively (Fig. 2; [3]). In northeast Taiwan, where the strike of the Ryukyu arc (~E–W) is approximately perpendicular to the regional structural trend, the effect of collision is prominent in the subducted Philippine Sea plate beneath the Ryukyu arc, and has resulted in the clockwise rotation of major geological structures [4]. In contrast, in south Taiwan where the strike of north Luzon arc is roughly parallel to the trend of major structure, no clear collision effects occur within the subducted Eurasian plate, and the subduction-related signatures gradually disappear northward [5]. Within such a complex tectonic framework, study of the structure and deformation of the Taiwan orogen is critical to understanding the tectonic processes responsible for the uplift of the Taiwan

\* Corresponding author. Tel.: +886-6-238-3399;  
Fax: +886-6-209-9733; E-mail: rau@mail.sgrc.ncku.edu.tw

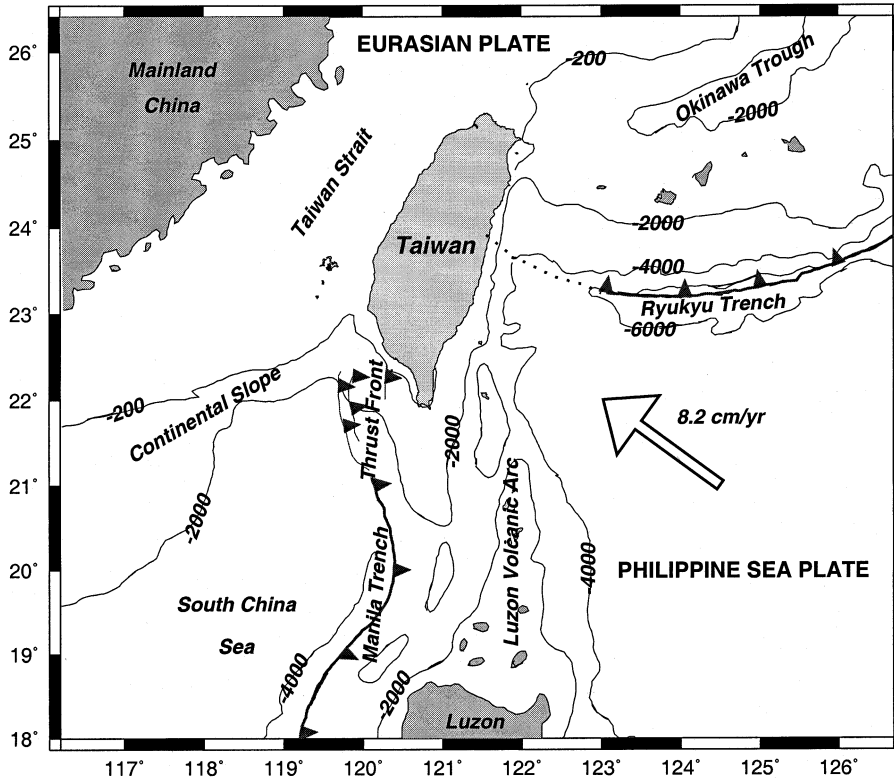


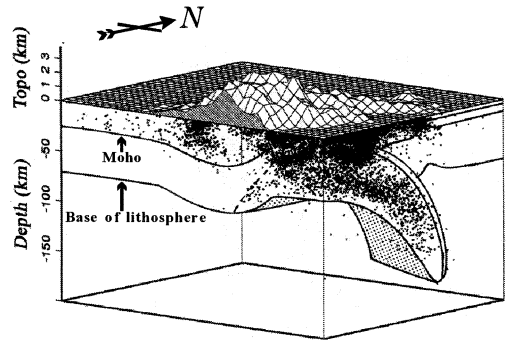
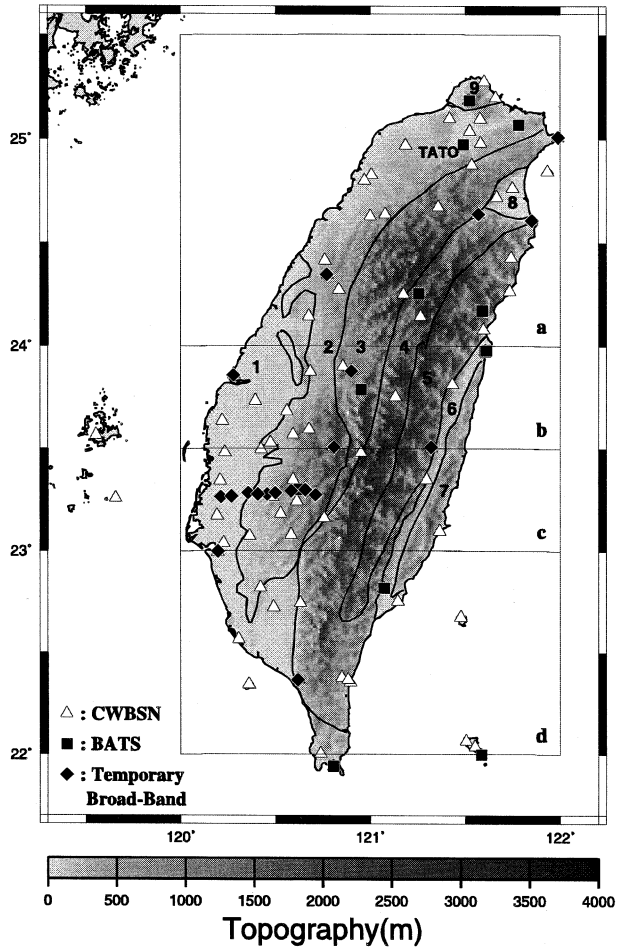
Fig. 1. Overall plate tectonic environment of Taiwan (modified from [26]). Arrow shows vector of relative motion between Philippine Sea plate and Eurasian plate [2].

mountain belts. In turn, such study would be valuable in deciphering the geodynamic development of modern orogenies. Through observations of seismic anisotropy, the purpose of this paper is to constrain the mode of upper mantle deformation in the Taiwan orogeny by analyzing splitting in teleseismic shear waves recorded at the seismic stations in Taiwan.

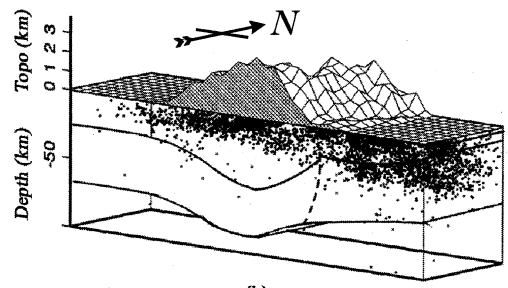
It is commonly accepted that the anisotropy, as revealed by teleseismic shear wave splitting, is closely related to the strain-induced lattice pre-

ferred orientation of upper mantle minerals [6]. Accordingly, the shear wave splitting parameters, the fast polarization direction,  $\phi$ , and the time delay,  $\delta t$ , between fast and slow shear waves, may indicate the mantle flow direction and the intensity of deformation, respectively [7]. At active collisional orogens (see [7]), shear wave splitting parameters generally follow a systematic pattern with  $\phi$  aligned parallel to the strike of the mountain belts and generally large  $\delta t$  (1.0–2.4 s). Based on these observations, it has been suggested

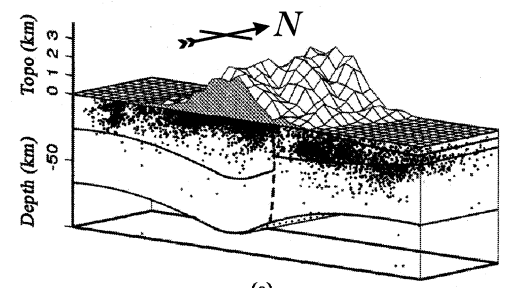
Fig. 2. (Left) Map of Taiwan showing locations of 75 short-period CWBSN seismic stations (empty triangles), 12 BATS stations (dark squares) and 19 temporary broad-band stations (dark diamonds). Main geologic boundaries and physiographic units [10]: 1. Western Coastal Plain, 2. Western Foothills, 3. Hsueshan Range, 4. Backbone Range, 5. Eastern Central Range, 6. Longitudinal Valley, 7. Coastal Range, 8. Ilan Plain, 9. Tatun volcanic group. Topography of Taiwan also shown. (Right) Synthesis of seismological and geophysical data showing major subsurface structures (modified from [3]). The structures are superposed on the three-dimensional seismic foci [26]. (a) Northeast Taiwan subduction zone. (b, c) Central Taiwan collision zones. (d) Southern Taiwan subduction–collision transition zone.



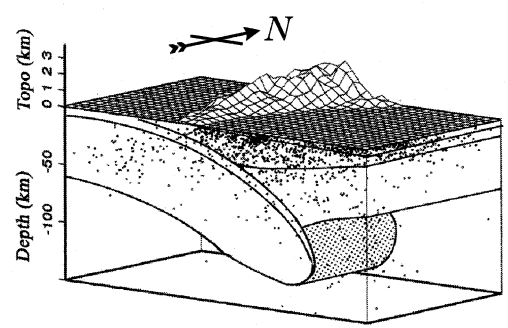
(a)



(b)



(c)



(d)

that a 100–200 km thickness of uppermost mantle materials beneath active collisional belts deforms coherently with the surface geologic fabric [7,8]. Although the coherent deformation mechanism is strongly supported by worldwide splitting observations [7], one better way to attest its viability is to examine spatial variations of splitting parameters in a small active orogen with well-defined surface geology and history, and dense closely monitored seismic stations [9]. Taiwan suits very well for such a study and offers an opportunity to investigate short-wavelength variations in seismic anisotropy beneath an active collisional orogen.

With the results obtained from shear wave splitting analyses, we wish to address the following questions related to the deformation mechanism of the Taiwan orogeny. First, is the orientation of  $\phi$  aligned parallel to the local structural fabric [10] and therefore reflecting vertical cou-

pling between mantle strain and crustal deformation? If such a coupling indeed exists, what is the intensity of mantle deformation in the Taiwan orogeny? Second, as the subducted Philippine Sea plate in northeast Taiwan has experienced significant collision effects in great depth, is the collision-induced clockwise rotation of major structures in northeast Taiwan reflected in the trend of  $\phi$ ? Finally, as the subduction effect is successively vanishing and the collision process has just begun in south Taiwan, how does mantle deformation change as the boundary changes from subduction to collision? Through a detailed analysis of shear wave splitting observations, our results indicate that, as manifested by orogen-parallel motion for the Taiwan mountain belt stations, lithospheric mantle strain is coherent with crustal deformation in the Taiwan orogeny. On the other hand, while the subduction-related

Table 1  
Event list

Event	Time (h:min:s)	Lat. (°N)	Lon. (°E)	Depth (km)	Mag. (mb)
910607	11:51:25.9	-7.20	122.53	536	6.2
921112	22:28:57.5	-22.40	-178.10	360	5.9
930321	05:04:59.1	-18.04	-178.53	589	6.1
930416	14:08:38.9	-17.78	-178.86	565	6.0
930420	16:26:19.5	-20.88	-178.70	592	5.6
930424	09:54:21.0	-17.87	179.85	599	5.5
931011	15:54:21.2	32.02	137.83	351	6.9
940331	22:40:52.1	-22.06	-179.53	580	6.1
940928	16:39:51.6	-5.79	110.35	638	6.6
950117	16:45:11.8	-20.83	-179.24	634	5.9
950413	02:34:37.9	-13.45	170.43	638	5.6
950816	15:04:01.3	-31.95	179.36	463	5.7
950823	07:06:02.7	18.86	145.22	595	6.8
950919	22:52:23.1	-39.70	174.17	217	5.8
960316	22:04:06.2	28.98	138.94	477	5.9
960617	11:22:18.5	-7.14	122.59	587	6.6
960720	07:41:15.2	-19.82	177.64	357	5.9
960827	06:24:07.9	-22.57	-179.79	575	5.6
961105	09:41:34.7	-31.16	180.00	369	5.9
961222	14:53:27.6	43.21	138.92	227	6.5
970321	12:07:17.6	-31.16	179.62	449	6.2
970904	04:23:37.0	-26.57	178.34	625	6.5
970907	12:57:06.7	-6.02	154.46	421	5.8
971017	15:02:00.4	-20.89	-178.84	579	6.0
980329	19:48:16.2	-17.55	-179.09	537	7.1
980414	03:41:22.3	-23.82	-179.87	499	6.1
980516	02:22:03.7	-22.20	-179.56	586	6.8
990408	13:10:34.0	43.60	130.53	560	7.2

upper mantle trench-parallel motion may remain in southernmost Taiwan, the deformation in the southern Taiwan subduction–collision transition zone is characterized by the diminishing of the subduction effect, followed by the initiation of a northward collision process.

## 2. Data and analysis

Data used in this study come from the short-period Central Weather Bureau Seismic Network (CWBSN; [11]; Fig. 2), the Broad-band Array in Taiwan for Seismology (BATS; [12]; Fig. 2) and two temporary broad-band arrays. BATS includes the only IRIS Global Seismic Network station in Taiwan, TATO (Taipei), which has been running since 1992 and therefore has recorded more data than the other Taiwan broad-band stations. Data sampling rates vary between 100 samples/s for CWBSN stations and 20 samples/s for broad-band stations. For studies of teleseismic shear wave splitting, SKS and SKKS phases observed at epicentral distances of 85–120° are the most frequently used phases because splitting of these phases is caused only by the receiver-side anisotropy [7]. Unfortunately, the SKS and SKKS phases recorded in the Taiwan region are usually of poor quality, probably due to no large-magnitude deep event occurred at the specified distance range, and the high level of microseismic noise resulting from the island nature of Taiwan. The deficiency of high quality SKS and SKKS phases is also no exception to the station TATO (see analysis below). As a result, all our data were taken from teleseismic ScS and S phases recorded from deep events with epicentral distances < 35° and 45–79°, respectively. The use of ScS arrivals from distances less than 35° is necessary to avoid problems with phase shifts at the reflection from the core–mantle boundary. The advantage of using S arrivals with distances between 45° and 79° is to allow near-vertical incidence and to limit interference of S with SKS and ScS phases. To minimize the source-side upper mantle/crustal anisotropy and to avoid contamination by sS, we use events with focal depths mostly greater than 350 km, except for two events having focal depths of

Table 2  
Station locations

Station	Lat. (°N)	Lon. (°E)	Location	Elev. (m)
<i>CWBSN</i>				
ALS	23.51	120.81	2	2413
CHK	23.10	121.37	7	34
CHN1	23.18	120.53	2	360
CHN4	23.35	120.59	2	205
CHN5	23.60	120.68	2	840
CHN8	23.35	120.21	1	6
EAS	22.38	120.85	4	445
ENA	24.43	121.74	5	113
ENT	24.64	121.57	8	280
HEN	22.01	120.74	1	–128
HSN	24.80	120.97	2	34
ILA	24.77	121.75	8	7
NSY	24.42	120.76	2	311
PNG	23.57	119.56	–	11
SCL	23.18	120.19	1	7
SCZ	22.37	120.62	4	74
SGL	22.73	120.49	1	30
SGS	23.08	120.58	2	277
TAI	23.00	120.20	1	14
TAW	22.36	120.90	4	8
TCU	24.15	120.68	1	84
TWA	24.98	121.58	2	260
TWB1	25.01	121.99	3	130
TWK1	21.94	120.81	1	90
TWL	23.27	120.49	2	590
TWU	24.88	121.53	3	330
TYC	23.90	120.86	3	20
WDT	23.76	121.13	4	2550
WGK	23.69	120.56	2	75
WNT	23.88	120.68	2	110
WSF	23.64	120.22	1	6
WTP	23.25	120.61	2	560
YUS	23.48	120.95	3	3845
<i>BATS</i>				
ANPB	25.19	121.52	9	825
HWAB	23.98	121.61	6	16
LYUB	22.00	121.58	–	40
NACB	24.18	121.59	5	130
SSLB	23.79	120.95	3	450
TATO	24.98	121.49	2	53
TDCB	24.26	121.26	4	1280
TPUB	23.30	120.63	2	370
TWGB	22.82	121.07	6	195
TWKB	21.94	120.81	1	90
WFSB	25.07	121.78	2	100
<i>Temporary broad-band</i>				
EHYB	23.51	121.32	5	237
WTCB	23.86	120.28	1	4
C014	23.30	120.58	2	520
C045	23.30	120.66	2	500
C050	23.28	120.41	2	120
C055	23.27	120.27	1	7

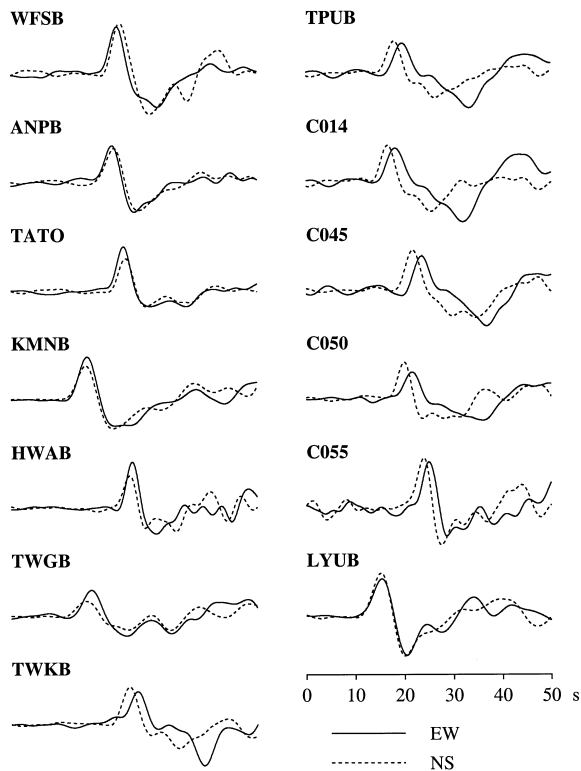


Fig. 3. Examples of broad-band S seismograms for event 980329 showing variations in time separations between S arrivals on the two horizontal components.

~ 220 km. Table 1 shows a list of all events used in this study. We visually inspected all events and we only analyzed S or ScS phases with excellent signal-to-noise ratios. The waveforms analyzed have signal periods of 1.3–2 s and 10–16 s for ScS and S phases, respectively. In total, we selected 38 ScS and 49 S phases from 28 earthquakes and 50 stations (Table 2). To remove unwanted noise, the seismograms were band-pass-filtered at 0.5–5 Hz for ScS and at 0.02–0.14 Hz for teleseismic S, respectively. Figs. 3 and 4 show examples of S and ScS phases on the horizontal seismograms recorded from two selected events: variations in time separations between arrivals of shear waves on the two horizontal components, indicating differences in splitting parameters, are clearly identified among different stations.

We measure the splitting parameters ( $\phi$ ,  $\delta t$ ) of teleseismic ScS and S phases by applying particle

motion analysis and using the cross-correlation method [13] assuming that the splitting is generated by a single anisotropic layer. For the cross-correlation method, the two horizontal seismograms are rotated in the horizontal plane at a 1° increment from -90° to 90°. The seismograms are then cross-correlated in the selected S wave time window, with an increment time shift of 0.01 and 0.05 s from 0 to 3 s for ScS and S, respectively. When the absolute value of the cross-correlation coefficient reaches its maximum, the rotation direction is chosen for the fast polarization direction ( $\phi$ ) and the time lag ( $\delta t$ ) is measured as the delay time of the slow shear wave. The results are accepted only when the absolute value of the maximum cross-correlation coefficient is > 0.9. The 95% confidence interval of the solution is estimated by using the interval estimate for the

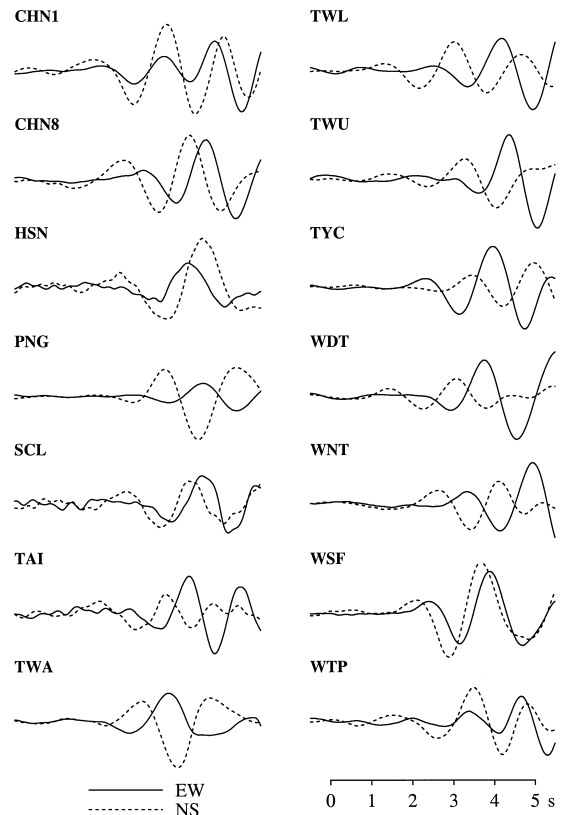
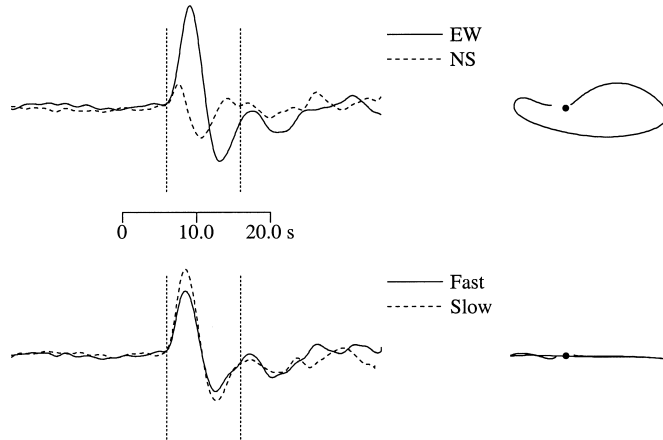


Fig. 4. Examples of short-period ScS seismograms for event 950823.

(a) TATO\_960827



(b)

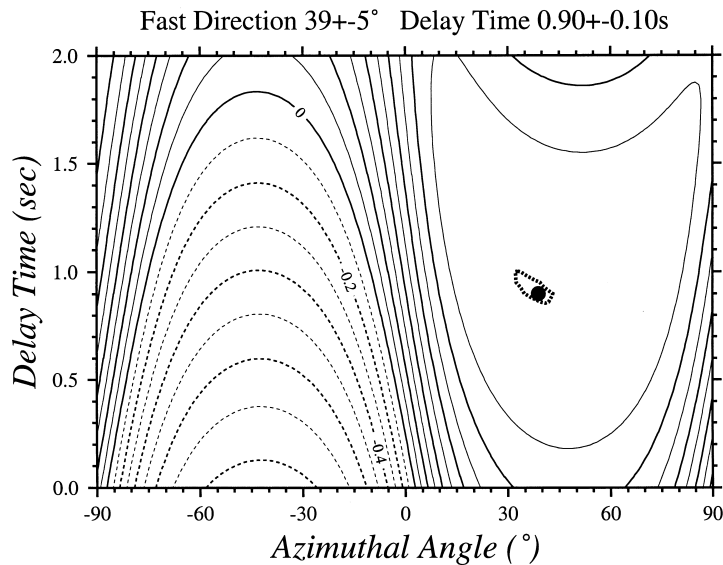
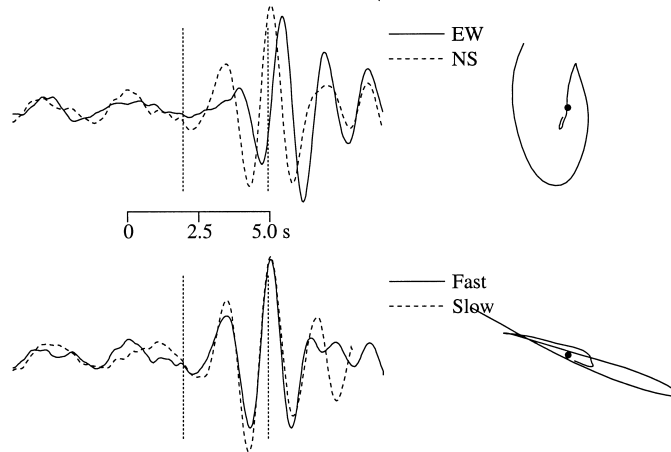


Fig. 5. An example of measurement from an S wave recorded at station TATO for event 960827. (a) Upper two traces are the superposition of E–W (solid line) and N–S (dashed line) components. Lower two are the corrected fast (solid line) and slow (dashed line) components. Vertical dashed lines on the seismograms mark the intervals used to make the measurements. Corresponding particle motions are shown on the upper right panel. (b) A diagram of the distribution of the cross-correlation coefficients in  $(\phi, \delta t)$  space. The estimated solution corresponding to the maximum value (dot) is shown with 95% confidence region (thick dashed line); dashed contour indicates negative coefficient.

cross-correlation coefficient ([14], see Appendix). Two examples of splitting measurements are shown in Figs. 5 and 6. The measurements demonstrate similar pulse shapes for the two horizon-

tal seismograms and produce linear particle motion after correction of anisotropic effects. A few good ScS and S null measurements are also obtained, which are consistent with the absence of

## (a) CHN8\_950823



## (b)

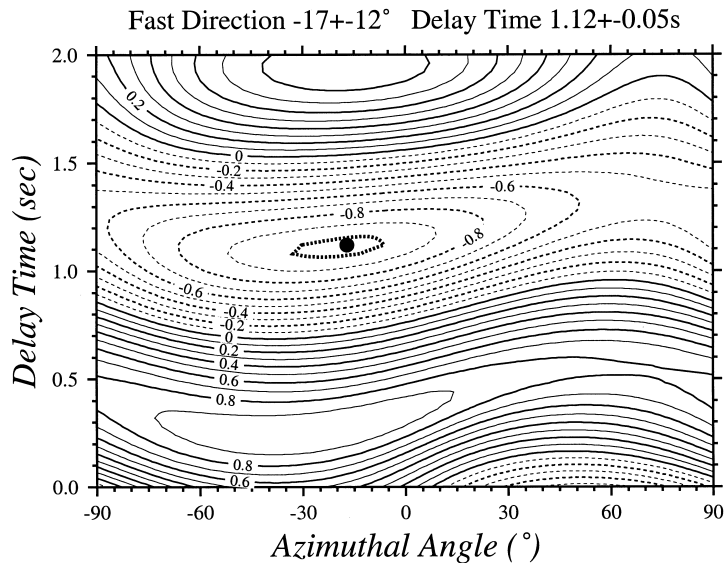


Fig. 6. Example of measurement from an ScS wave recorded at station CHN8 for event 950823. The symbols and format are the same as Fig. 5.

anisotropy, or a polarization direction close to the fast or slow axes.

Among the stations we studied, TATO has a longer recording history, and thus we examine the consistency of splitting parameters for both S and SKS obtained at this station in detail. TATO is situated in the Western Foothills area and is located just  $\sim 10$  km west of the northeast-

ern Taiwan subduction zone system (Fig. 2). The local mountain ranges tend to strike  $\sim N55^\circ E$ . Similar to the other Taiwan broad-band stations, S events of TATO are clustered at back-azimuths of  $120^\circ$ – $133^\circ$  recorded from Fiji–Tonga subduction zone earthquakes. Among the splitting parameters of S events obtained for TATO (Table 3), only five of 19 event solutions show clear split-

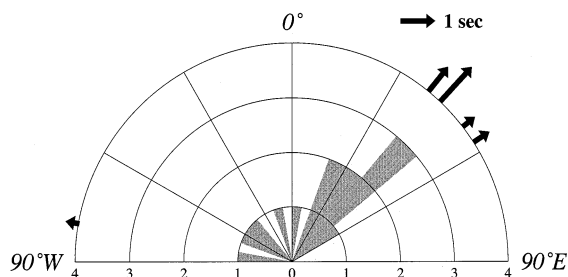


Fig. 7. Distribution of incoming polarizations for null measurements of TATO. Each sector represents the amount, as shown in radius, of null measurements averaged within  $10^\circ$  azimuths. Incoming polarizations are clustered mainly on  $45^\circ$ ; consistent with most fast polarizations (dark arrows on the ring of rose diagram) observed for non-null measurements.

ting; 14 are null measurements. Of the five split events, all but one ( $-80^\circ$ , 0.4 s) have  $\phi$  centered on  $48^\circ$  ( $39^\circ$ – $57^\circ$ ), sub-parallel to the trend of local mountain belts, but  $\delta t$ s vary greatly (0.45–1.35 s). The null measurements were obtained at incoming polarizations mostly of  $45^\circ$ ; close to the average fast direction (Fig. 7). With a limited back-azimuth coverage, splitting parameters of S events at TATO are indicated by four consistent splitting measurements, supported by nulls at initial polarizations where splitting should not be seen. As for the SKS and SKKS events of TATO, there are nearly 100 events satisfying our event selection criteria (see data section above). However, for these events, the noise levels for SKS and SKKS phases on the transverse components are generally too high, such that we can hardly distinguish signal from noise on the seismograms.

To assess the degree of heterogeneity of the anisotropic layer and the lateral or radial variations of the structures, we test the frequency dependence in the shear wave splitting parameters [15]. We filtered the shear wave phase using narrow-band-pass filters and constant width frequency limits, and determined the splitting parameters correspondingly. By moving the band-pass window in the frequency domain, we investigated possible variations in the splitting parameters as a function of the dominant signal frequency. For both S and ScS waveforms, we found no significant variation in the splitting parameters (both  $\phi$  and  $\delta t$ ) as a function of the

dominant signal frequency, suggesting fairly homogeneous anisotropic structures.

### 3. Regional patterns of splitting parameters

Splitting parameters from teleseismic ScS and S phases are shown in Table 3 and Fig. 8. While the ScS events cover a broader range of back-azimuth ( $\sim 200^\circ$ ; Fig. 9), the S events are clustered at a limited back-azimuth range of  $23^\circ$  (from  $119^\circ$  to  $142^\circ$ ). Although only a few observations are available for most events, both  $\phi$  and the magnitude of  $\delta t$  are generally consistent for the stations located in the same tectonic regime. However, for some measurements within these regions, S delay times are generally larger than that of ScS; this is most prominent for stations in southwestern Taiwan (Fig. 8 and  $\sim 25$  km north of C profile in Fig. 10). This discrepancy is probably due to differences in incidence angles between S and ScS phases. Compared to near-vertically incident ScS phases, the more shallow incident S phase may sample a longer anisotropy path length in the upper mantle beneath the receivers assuming horizontally layered anisotropy. Furthermore, because the numbers of splitting solutions are very limited for each station, we did not calculate mean splitting parameters at each site and we present all the results for each station.

We examine splitting parameters obtained for Taiwan seismic stations in three regions: the collision orogen in central Taiwan, and the subduction–collision systems in northeast and south Taiwan, respectively (Fig. 2). In the central Taiwan collision orogen, most of the stations are characterized by  $\phi$  trending N15°W to N25°E, and relatively large  $\delta t$  of 1.0–2.1 s for S arrivals, and 0.7–1.5 s for ScS arrivals. The trends of  $\phi$  are approximately parallel to the strike of the mountain belts and perpendicular to the direction of relative plate motion between the Eurasian plate and the Philippine Sea plate. No systematic variation of  $\delta t$  for both S and ScS can be observed across central Taiwan.

At stations situated right above the northeast Taiwan subduction zone,  $\phi$  trends nearly E–W and is roughly trench-parallel. However, for the

Table 3  
Splitting parameters

Station	Event	Phase	Baz (°)	Pol. (°)	$\phi$ (°)	$\delta t$ (s)
ALS	961222	ScS	33	56	$6 \pm 15$	$1.36 \pm 0.07$
ALS	990408	ScS	19	-30	-	-
CHK	990408	ScS	18	-22	-	-
CHN1	950823	ScS	96	21	-	-
CHN4	960316	ScS	67	63	$10 \pm 11$	$1.58 \pm 0.05$
CHN5	990408	ScS	20	22	$-37 \pm 7$	$0.52 \pm 0.05$
CHN8	950823	ScS	96	-74	$-16 \pm 11$	$1.12 \pm 0.05$
EAS	990408	ScS	18	-33	$7 \pm 25$	$0.48 \pm 0.05$
ENA	940928	ScS	202	30	$39 \pm 20$	$1.24 \pm 0.20$
ENA	990408	ScS	19	-6	$29 \pm 35$	$0.44 \pm 0.15$
ENT	990408	ScS	19	-61	-	-
HEN	990408	ScS	18	38	$-20 \pm 10$	$1.22 \pm 0.05$
HSN	950823	ScS	100	11	$57 \pm 25$	$0.28 \pm 0.08$
ILA	990408	ScS	19	55	$-77 \pm 20$	$0.68 \pm 0.05$
NSY	910607	ScS	177	56	$25 \pm 15$	$0.76 \pm 0.15$
PNG	950823	ScS	96	-14	-	-
SCL	950823	ScS	96	-68	$-10 \pm 7$	$1.00 \pm 0.03$
SCZ	990408	ScS	19	2	-	-
SGL	910607	ScS	176	26	$-8 \pm 16$	$0.40 \pm 0.10$
SGS	910607	ScS	176	35	$36 \pm 6$	$0.75 \pm 0.10$
SGS	990408	ScS	20	-48	$-9 \pm 30$	$1.36 \pm 0.10$
TAI	950823	ScS	95	-68	$-15 \pm 20$	$1.20 \pm 0.05$
TAW	910607	ScS	177	69	$23 \pm 13$	$0.39 \pm 0.10$
TCU	910607	ScS	176	67	$23 \pm 15$	$0.67 \pm 0.10$
TWA	950823	ScS	101	-33	$83 \pm 10$	$0.28 \pm 0.05$
TWB1	960617	ScS	179	-46	$-88 \pm 30$	$1.17 \pm 0.05$
TWK1	990408	ScS	18	-31	$20 \pm 12$	$0.94 \pm 0.05$
TWL	940928	ScS	200	60	$8 \pm 15$	$0.48 \pm 0.10$
TWL	950823	ScS	96	62	$11 \pm 11$	$1.08 \pm 0.05$
TWU	950823	ScS	101	79	$13 \pm 12$	$1.04 \pm 0.10$
TYC	950823	ScS	98	-82	-	-
WDT	950823	ScS	96	-71	$1 \pm 18$	$1.44 \pm 0.08$
WGK	910607	ScS	176	61	$-8 \pm 12$	$0.73 \pm 0.10$
WNT	931011	ScS	58	37	$0 \pm 5$	$0.76 \pm 0.05$
WNT	950823	ScS	98	-70	$-18 \pm 5$	$1.52 \pm 0.05$
WSF	950823	ScS	97	35	-	-
WTP	950823	ScS	96	64	$26 \pm 7$	$1.04 \pm 0.10$
YUS	990408	ScS	19	-25	$31 \pm 7$	$1.34 \pm 0.05$
ANPB	980329	S	120	47	$82 \pm 20$	$0.55 \pm 0.20$
ANPB	980414	S	126	48	-	-
LYUB	970907	S	127	31	$-12 \pm 18$	$0.60 \pm 0.30$
LYUB	980329	S	119	41	-	-
NACB	950919	S	142	28	-	-
NACB	960827	S	125	70	$7 \pm 23$	$1.90 \pm 0.65$
TATO	921112	S	124	-45	-	-
TATO	930321	S	120	7	-	-
TATO	930416	S	120	38	-	-
TATO	930420	S	123	40	-	-
TATO	930424	S	121	37	-	-
TATO	931011	S	120	41	-	-
TATO	940331	S	124	-17	-	-
TATO	950117	S	123	24	-	-
TATO	950413	S	123	-67	-	-

Table 3 (continued)

Station	Event	Phase	Baz (°)	Pol. (°)	$\phi$ (°)	$\delta t$ (s)
TATO	950816	S	133	20	–	–
TATO	960720	S	121	53	–	–
TATO	960827	S	125	–88	$39 \pm 5$	$0.90 \pm 0.10$
TATO	961105	S	132	5	$57 \pm 20$	$0.55 \pm 0.20$
TATO	970321	S	132	–86	$52 \pm 20$	$0.45 \pm 0.30$
TATO	970904	S	129	–86	–	–
TATO	971017	S	123	–53	–	–
TATO	980329	S	120	52	$-80 \pm 15$	$0.40 \pm 0.20$
TATO	980414	S	126	46	–	–
TATO	980516	S	124	11	$43 \pm 25$	$1.35 \pm 0.45$
TDCB	960720	S	121	47	$2 \pm 20$	$0.90 \pm 0.40$
TDCB	970907	S	129	16	$-29 \pm 15$	$0.75 \pm 0.20$
TDCB	980414	S	126	33	$0 \pm 20$	$1.35 \pm 0.50$
TPUB	950919	S	141	61	$10 \pm 20$	$2.60 \pm 0.30$
TPUB	960720	S	120	51	$5 \pm 10$	$1.85 \pm 0.25$
TPUB	980329	S	119	34	$-5 \pm 16$	$1.85 \pm 0.40$
TPUB	980414	S	125	40	$6 \pm 8$	$2.15 \pm 0.30$
TWGB	960720	S	120	50	$9 \pm 20$	$1.05 \pm 0.45$
TWGB	970907	S	127	32	–	–
TWGB	980329	S	119	60	$0 \pm 20$	$1.05 \pm 0.30$
TWKB	980329	S	119	40	$1 \pm 15$	$1.60 \pm 0.25$
TWKB	980414	S	125	35	$8 \pm 18$	$1.45 \pm 0.35$
WFSB	980329	S	120	41	$80 \pm 15$	$0.80 \pm 0.25$
WFSB	980414	S	126	31	$81 \pm 12$	$0.45 \pm 0.35$
EHYB	950919	S	141	57	$0 \pm 20$	$1.20 \pm 0.80$
HWAB	980329	S	120	56	$12 \pm 18$	$0.65 \pm 0.20$
HWAB	980414	S	126	48	–	–
WTCB	950816	S	132	16	$-32 \pm 17$	$0.95 \pm 0.35$
C014	980329	S	119	37	$1 \pm 20$	$1.85 \pm 0.50$
C045	980329	S	119	31	$-10 \pm 12$	$1.85 \pm 0.25$
C045	980414	S	125	17	$-16 \pm 15$	$1.85 \pm 0.45$
C050	980329	S	119	32	$4 \pm 20$	$1.95 \pm 0.55$
C050	980414	S	125	36	$-4 \pm 10$	$1.30 \pm 0.30$
C055	980329	S	119	61	$7 \pm 15$	$1.30 \pm 0.25$

stations located just west of the western boundary of the subduction zone,  $\phi$  rotates to N40°E. This distinct change in the trends of  $\phi$  not only occurs at the transition from subduction to collision, but also corresponds to the rotation of the structural trend of the northern Taiwan mountain belt. In comparison to the central Taiwan collision orogen,  $\delta t$  for the northern Taiwan subduction–collision system is considerably smaller on average ( $\sim 0.7$  s).

Fast directions for the southern Taiwan stations are rather consistent and centered on N–S (from  $-20^\circ$  to  $20^\circ$ ). From southernmost Taiwan to  $\sim 40$  km northward, although the orientations of  $\phi$  are similar, average  $\delta t$  decreases from 1.5 s to

0.5 s. Compared to the fairly consistent  $\delta t$  for the stations in the central Taiwan collision zone, the change in  $\delta t$  at the southern Taiwan stations suggests that a fundamental change in the strength of anisotropy occurs in this subduction–collision transition system.

#### 4. Discussion

In general, the splitting parameters derived from the S phases are fairly consistent with those from the ScS, especially for the trends of  $\phi$ . Furthermore, within given tectonic regions, the orientations of  $\phi$  at different stations are consistent as

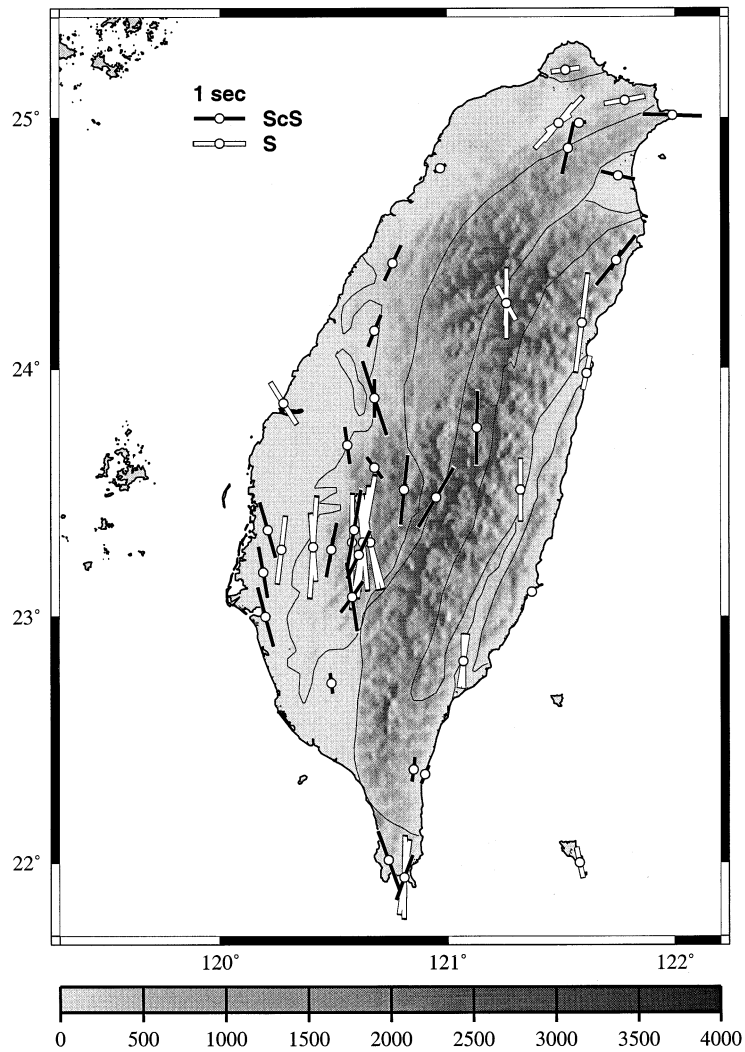


Fig. 8. Shear wave splitting parameters for both S and ScS phases plotted as vectors at station sites. Fast polarization directions are given by bar azimuth from north. Delay time is proportional to bar length, as given by scale bars. Topography of Taiwan also shown.

well for a wide range of back-azimuth (from  $18^\circ$  to  $202^\circ$ ), indicating that the anisotropy beneath Taiwan is rather homogeneous. However, a significant variation of  $\delta t$  from one tectonic region to another is also observed, ranging from 0.5 to 2.1 s. The short-wavelength variations in  $\delta t$  suggest that anisotropy beneath the Taiwan region is of shallow, predominantly lithospheric, origin based on the assumption of one source layer. From south to north, the orientations of  $\phi$  are, in general, parallel to the axes of the deforma-

tional belts and show a clockwise rotation of  $\sim 40^\circ$  in northeast Taiwan. The structural trends deviate from local  $\phi$  by  $< 20^\circ$ , with a mean deviation of  $\sim 15^\circ$ , which is about the average standard deviation of  $\phi$  (Fig. 10). The coherence between  $\phi$  and surface geologic features is consistent with the hypothesis that the splitting orientation is imparted through homogeneous deformation during collision events, and that the mantle deformation in the Taiwan orogen is directly coupled to the overlying crustal shortening.

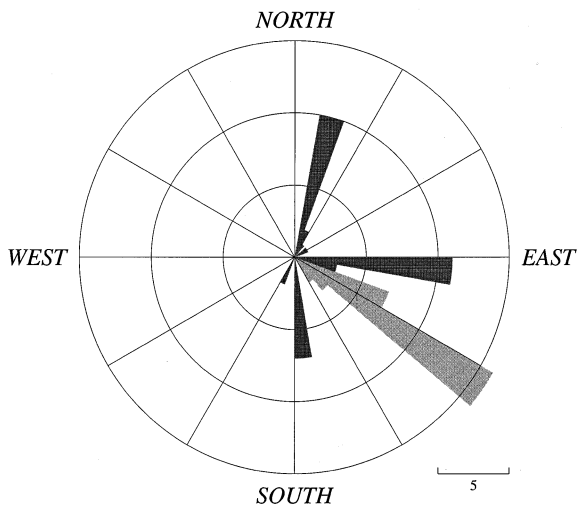


Fig. 9. Rose diagram showing earthquake back-azimuth distribution. Each ring represents five measurements. Dark and gray sectors, averaged within  $10^\circ$  azimuths, are for ScS and S events, respectively. While ScS events cover a broader range of back-azimuth ( $\sim 200^\circ$ ), S events are clustered at a limited back-azimuth range of  $23^\circ$  (from  $119^\circ$  to  $142^\circ$ ).

Such internally coherent deformation is commonly observed in active tectonic regions [7].

Although a single layer of anisotropy is our basic assumption, we cannot ignore the possibility that several layers of anisotropy may be present beneath Taiwan. Based on studies of the effect of several layers of anisotropy on the splitting measurements [16,17], the uppermost layer will control the trend of the measured anisotropy. If several layers of anisotropy did exist beneath Taiwan, the general parallelism of the anisotropy with the Taiwan orogen suggests that the anisotropy is indeed controlled by the uppermost mantle and that the Taiwan orogen is characterized by a strong coherent deformation of the upper mantle and the crust. Furthermore, while  $\phi$  is much more robust than  $\delta t$  for the splitting measurements of Taiwan, the complex behavior of  $\delta t$  is probably a result of several layers of anisotropy beneath Taiwan and part of  $\delta t$  may be acquired from the source-side anisotropy. Unfortunately, we do not have stations with enough data and with good back-azimuthal coverage to detect possible back-azimuthal dependence of the splitting parameters, such that we cannot evaluate the pos-

sibility of several layers of anisotropy beneath Taiwan.

Due to their near-vertical incidence, splitting parameters of S and ScS phases provide excellent lateral resolution beneath the stations. However, they lack vertical resolution and fail to constrain the depth extent of anisotropy. Moreover, unlike the SKS/SKKS events, although we use deep-focus events, we cannot preclude the possibility that the splitting parameters derived from S and ScS events may carry source-side anisotropy in some regions [18,19]. Nevertheless, it is generally agreed that splitting due to lower mantle anisotropy is negligible [20–22] and the split times in the crust are mostly less than about 0.2 s [7]. As a result, the upper mantle beneath Taiwan is likely to be the major source of anisotropy. Based on Fresnel zone calculations [23], and given station spacing of 10–40 km, the observed variations in splitting parameters in the Taiwan orogen place a lower limit on the depth of the anisotropic layer at about 250 km. Assuming an intrinsic shear wave velocity anisotropy of 4%, which corresponds to the average anisotropy of naturally occurring peridotites [24,25], 1 s of splitting time corresponds to an anisotropic layer thickness of 115 km. Thus, splitting across Taiwan suggests an anisotropic layer thickness of 25–230 km in the uppermost mantle. While longer  $\delta t$ s (1.5–2 s), and therefore larger thickness (173–230 km), are observed in central Taiwan orogen, thinner layers of 60 and 25 km are inferred for the northeast and south Taiwan subduction–collision transition zones, respectively. The observed variations in  $\delta t$  correlate well with the lithospheric structure, where the central Taiwan has thicker lithosphere compared with the surrounding regions [26].

A more unique and important question in studying the Taiwan collision is how the mantle deforms as the boundary changes from collision to subduction in northeast and south Taiwan, respectively. In northeast Taiwan, lying above the back-arc region of the Ryukyu subduction zone, fast directions show a clockwise rotation following the general trend of local structures. The apparent correlation of fast directions with local structure and the smaller split times observed in north Taiwan are compatible with a lithospheric

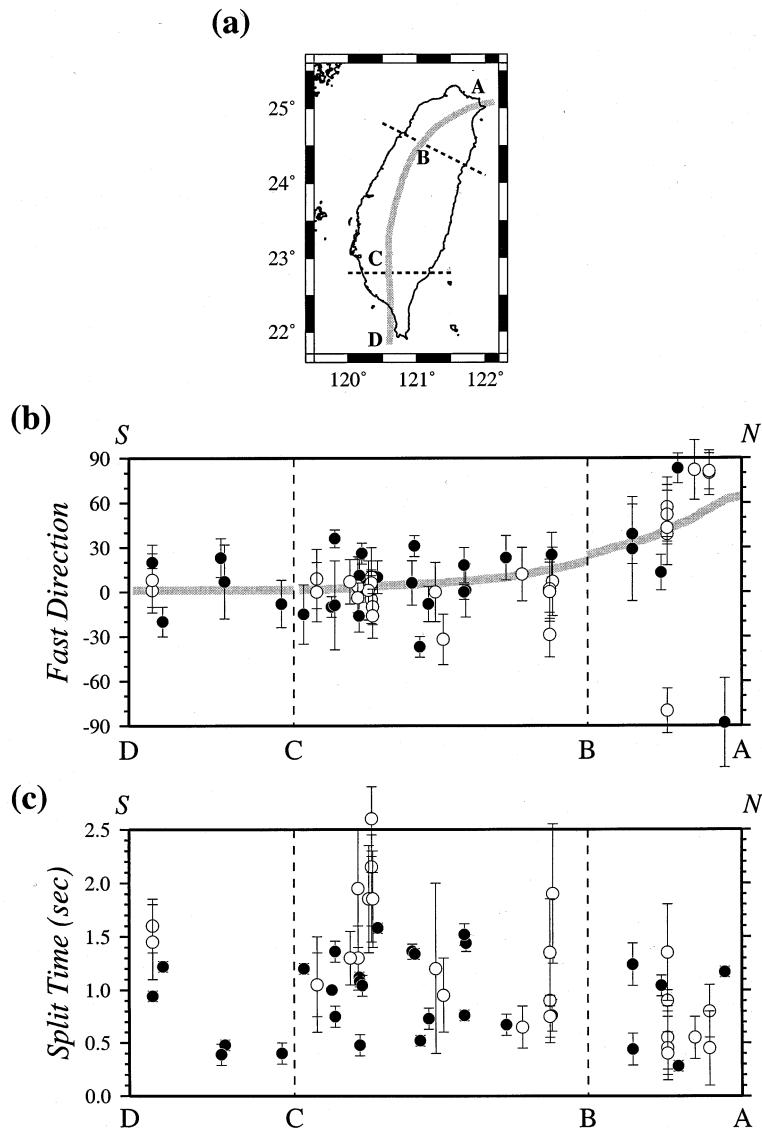


Fig. 10. Variations of splitting parameters along strike of the structural trend of Taiwan. (a) Map of Taiwan showing strike of major structure (gray line). The island is separated into three parts: north (A–B), central (B–C) and south (C–D) Taiwan. (b) Variations of fast directions along strike (gray line). Open and dark circles represent S and ScS measurements, respectively. Estimated error for fast direction is marked for each measurement. (c) Variations of delay times along strike. Symbols, the same as (b).

origin of the anisotropy. This lithospheric anisotropy probably results from the rigorous lithospheric collision between the Ryukyu slab and the Chinese continental margin [4]. A study using direct S waves from the subducted Ryukyu slab is needed to constrain the exact source of anisotropy further.

In southernmost Taiwan, the  $\delta t$  is relatively large and  $\phi$  is N–S, parallel to both the structural trend and the trench axis. However,  $\sim 40$  km north of southernmost Taiwan, although the orientations of  $\phi$  remain N–S,  $\delta t$  decreases sharply from 1.3 to 0.5 s. This abrupt change is probably associated with the diminishing subduction effect

and the commencement of collision processes. Although the anisotropy for southernmost Taiwan is trench-parallel, as commonly observed for most subduction zone fore-arc regions [18], further investigation using direct S waves from the subducted Eurasia slab may be able to pinpoint the exact source of anisotropy there.

## 5. Conclusions

The orientations of anisotropy from the Taiwan stations generally follow the trend of regional geological structures, indicating vertically coherent deformation between mantle flow and overlying crustal shortening beneath Taiwan orogen. The delay times vary significantly from 0.5 to 2.1 s; the largest values are from southwestern Taiwan foothills and an abrupt change in delay times is found in south Taiwan. This suggests different intensities of deformation along the strike of the Taiwan mountain belt. The main source of shear wave splitting in Taiwan is an anisotropic region between 25 and 230 km depths, which is of lithospheric origin.

## Acknowledgements

We thank the staff of the Seismology Center of the Central Weather Bureau and the Institute of Earth Sciences, Academia Sinica, for providing high quality earthquake data used in this research. We also thank B.-Y. Kuo for stimulating discussions. The manuscript benefited from the constructive comments of Ray Russo and an anonymous reviewer. The research was partially supported by the Institute of Earth Sciences, Academia Sinica, and the Satellite Geoinformatics Research Center, National Cheng Kung University, Taiwan. [RV]

## Appendix. Interval estimate for the correlation coefficient

The confidence interval estimation used in [14] adopted the method described in [27]. Since there

is no direct way to estimate the correlation coefficient  $\rho$  of a two-dimensional normal distribution, we proceed in an indirect way. From the maximum correlation coefficient  $r$  in  $(\phi, \delta t)$  domain as shown in Fig. 5, we first compute the auxiliary value:

$$z_0 = \frac{1}{2} \ln \frac{1+r}{1-r} \quad (1)$$

where  $z_0$  is an estimate for the mean:

$$\mu^* = \frac{1}{2} \ln \frac{1+\rho}{1-\rho} \quad (2)$$

of a random variable  $Z$ , which is asymptotically normal and has variance:

$$\sigma^{*2} = \frac{1}{n-3} \quad (3)$$

where  $n$  is the degree of freedom of sample. We further define  $n$  as half the sample size, assuming it is independent of all the other data points. After such a transformation, we follow the method commonly used for the mean of a normal distribution to give an estimate for the correlation coefficient of a two-dimensional normal distribution, such that  $z_0$  plays the role of the sample mean, and we now have  $\sigma^* = 1/\sqrt{n-3}$ . By doing so, we obtain a confidence interval for  $r$  through the estimation of the confidence interval for  $\mu^*$ . In this way, we first obtain the confidence interval:

$$\text{CONF}\{z_0 - k \leq \mu^* \leq z_0 + k\}, \text{ where } k = \frac{c}{\sqrt{n-3}} \quad (4)$$

and values of  $c$  are 1.645, 1.960, 2.576 and 3.291 for confidence levels of 90, 95, 99 and 99.9%, respectively. Here,  $c$  is selected as 1.960 corresponding to 95% confidence level. We then convert this interval into an interval for  $\rho$  of the form:

$$\text{CONF}\{r_1 \leq \rho \leq r_2\} \quad (5)$$

where:

$$r_1 = \tan h(z_0 - k) \text{ and } r_2 = \tan h(z_0 + k) \quad (6)$$

Because the correlation coefficient of population  $\rho$  is estimated from the maximum value of the sample correlation coefficient, only the lower confidence limit,  $r_1$ , is desired for the estimation of the 95% confidence interval. We contour  $r_1$  on the  $(\phi, \delta t)$  domain to frame the 95% confidence region as shown in Fig. 5. This region is, however, an ellipse-like shape rather than a box shape. To give a more rigorous constraint, we use the extreme values of the border of confidence region to assign the measurement errors for both  $\phi$  and  $\delta t$ . Solutions with 95% confidence region containing zero delay time or extending more than 90° for azimuthal angles are rejected.

## References

- [1] J. Suppe, The active Taiwan mountain belt, in: J.P. Schaer and J. Rodgers (Eds.), *The Anatomy of Mountain Ranges*, Princeton Univ. Press, Princeton, 1987, pp. 277–293.
- [2] S.-B. Yu, H.-Y. Chen, L.-C. Kuo, Velocity field of GPS stations in the Taiwan area, *Tectonophysics* 274 (1997) 41–59.
- [3] F.T. Wu, R.-J. Rau, D.H. Salzberg, Taiwan orogeny: thin-skinned or lithospheric collision?, *Tectonophysics* 274 (1997) 191–220.
- [4] H. Kao, S.-S. Shen, K.-F. Ma, Transition from oblique subduction to collision: earthquakes in the southernmost Ryukyu arc-Taiwan region, *J. Geophys. Res.* 103 (1998) 7211–7229.
- [5] H. Kao, G.-C. Huang and C.-S. Liu, Transition from oblique subduction to collision in the northern Luzon arc-Taiwan region: constraints from bathymetry and seismic observations, *J. Geophys. Res.* (2000) (in press).
- [6] A. Nicolas and N.I. Christensen, Formation of anisotropy in upper mantle peridotites - A review, in: K. Fuchs and C. Froidevaux (Eds.), *Composition, Structure and Dynamics of the Lithosphere–Asthenosphere System*, American Geophysical Union, Washington, DC, 1987, pp. 111–123.
- [7] P.G. Silver, Seismic anisotropy beneath the continents: Probing the depths of geology, *Annu. Rev. Earth Planet. Sci.* 24 (1996) 385–432.
- [8] A. Vauchez, A. Nicolas, Mountain building strike-parallel motion and mantle anisotropy, *Tectonophysics* 185 (1991) 183–191.
- [9] G. Barruol, A. Souriau, A. Vauchez, J. Diaz, J. Gallart, J. Tubia, J. Cuevas, Lithospheric anisotropy beneath the Pyrenees from shear wave splitting, *J. Geophys. Res.* 103 (1998) 30039–30053.
- [10] C.S. Ho, An introduction to the geology of Taiwan: explanatory text of the geologic map of Taiwan, Ministry of Economic Affairs, Taipei, 1988, 192 pp.
- [11] T.-C. Shin, The calculation of local magnitude from the simulated Wood–Anderson seismograms of the short-period seismograms in the Taiwan area, *TAO* 4 (1993) 155–170.
- [12] H. Kao, P.-R. Jian, K.-F. Ma, B.-S. Huang, C.-C. Liu, Moment-tensor inversion for offshore earthquakes east of Taiwan and their implications to regional collision, *Geophys. Res. Lett.* 25 (1998) 3619–3622.
- [13] Y. Fukao, Evidence from core-reflected shear waves anisotropy in the Earth's mantle, *Nature* 309 (1984) 695–698.
- [14] W.-T. Liang, Shear wave splitting in northern Taiwan: Implications for crustal anisotropy, Master's thesis (in Chinese), National Taiwan University, 1990, 95 pp.
- [15] K. Marson-Pidgeon, M.K. Savage, Frequency-dependent anisotropy in Wellington, New Zealand, *Geophys. Res. Lett.* 24 (1997) 3297–3300.
- [16] G. Rumpker, P.G. Silver, Apparent shear-wave splitting parameters in the presence of vertically-varying anisotropy, *Geophys. J. Int.* 135 (1998) 790–800.
- [17] G. Rumpker, A. Tommasi, J.-M. Kendall, Numerical simulations of depth-dependent anisotropy and frequency-dependent wave propagation effects, *J. Geophys. Res.* 104 (1999) 23141–23153.
- [18] M.J. Fouch, K.M. Fischer, Mantle anisotropy beneath northwest Pacific subduction zones, *J. Geophys. Res.* 101 (1996) 15987–16002.
- [19] M.K. Savage, Seismic anisotropy and mantle deformation: What have we learned from shear wave splitting?, *Rev. Geophys.* 37 (1999) 65–106.
- [20] S. Kaneshima, P.G. Silver, Anisotropic loci in the mantle beneath central Peru, *Phys. Earth Planet. Int.* 88 (1995) 257–272.
- [21] C. Meade, P.G. Silver, S. Kaneshima, Laboratory and seismological observations of lower mantle isotropy, *Geophys. Res. Lett.* 22 (1995) 1293–1296.
- [22] K.M. Fischer, D.A. Wiens, The depth distribution of mantle anisotropy beneath the Tonga subduction zone, *Earth Planet. Sci. Lett.* 142 (1996) 253–260.
- [23] D. Alsina, R. Snieder, Small-scale sublithospheric continental mantle deformation: constraints from SKS splitting observations, *Geophys. J. Int.* 123 (1995) 431–448.
- [24] D. Mainprice, P.G. Silver, Interpretation of SKS-waves using samples from the subcontinental lithosphere, *Phys. Earth Planet. Int.* 78 (1993) 257–280.
- [25] W. BenIsmaïl, D. Mainprice, An olivine fabric database: An overview of upper mantle fabrics and seismic anisotropy, *Tectonophysics* 296 (1998) 145–157.
- [26] R.-J. Rau, F.T. Wu, Tomographic imaging of lithospheric structures under Taiwan, *Earth Planet. Sci. Lett.* 133 (1995) 517–532.
- [27] E. Kreyszig, *Introductory Mathematical Statistics, Principles and Methods*, John Wiley and Sons, 1970, 470 pp.